THE JOURNAL OF PHYSICAL CHEMISTRY C

pubs.acs.org/JPCC

Article

Growth of Supported Gold Nanoparticles in Aqueous Phase Studied by in Situ Transmission Electron Microscopy

Mark J. Meijerink, Krijn P. de Jong,* and Jovana Zečević*

Cite This: J. Phys. Chem. C 2020, 124, 2202–2212

Read Online

ACCESS | Metrics & More | Article Recommendations | Supporting Information

ABSTRACT: Nanoparticle growth has long been a significant challenge in nanotechnology and catalysis, but the lack of knowledge on the fundamental nanoscale aspects of this process has made its understanding and prediction difficult, especially in a liquid phase. In this work, we successfully used liquid-phase transmission electron microscopy (LP-TEM) to image this process in real time at the nanometer scale, using an Au/TiO_2 catalyst in the presence of $NaCl_{(aq)}$ as a case study. In situ LP-TEM clearly showed that the growth of Au nanoparticles occurred through a form of Ostwald ripening, whereby particles grew or disappeared, probably via monomer transfer, without clear correlation to particle size in contrast to predictions of classical Ostwald ripening models. In addition, the existence of a significant fraction of inert particles that neither grew nor shrank was observed. Furthermore, in situ transmission electron microscopy (TEM) showed that particle shrinkage was sudden and seemed a stochastic process, while particle growth by monomer attachment was slow and likely the rate-determining step for sintering in this system. Identification and understanding of these individual nanoparticle events are critical for extending the accuracy and predictive power of Ostwald ripening models for nanomaterials.

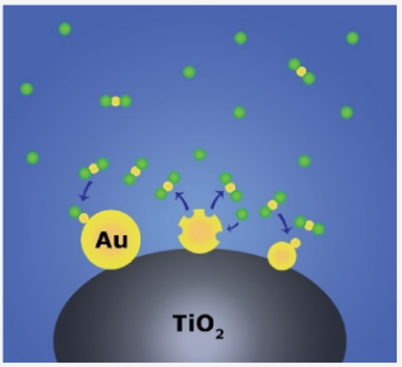

INTRODUCTION

In many fields, spanning from nanotechnology to targeted drug delivery and catalysis, controlling and maintaining the size of nanoparticles are considered crucial to preserve their unique size-dependent physicochemical properties.[1,2] Unfortunately, due to their small size and thus a high surface energy contribution to the thermodynamic potential, a large driving force for nanoparticle growth exists. As a result, nanoparticles grow (sinter) rapidly, often losing the desirable size-dependent properties in the process. This sintering is especially problematic in the field of heterogeneous catalysis, where chemical reactions are catalyzed at the particle surface. To maximize the available surface area and thus catalyst activity, particles should be and remain small (often <10 nm).[3]

Particle growth is therefore a significant challenge for heterogeneous catalysts, and for decades, researchers have been trying to understand underlying mechanisms and build kinetic models that explain and predict the sintering behavior.[4] This sintering is commonly considered to take place by Ostwald ripening (OR), by particle migration and coalescence, or as a result of a combination of both mechanisms. In OR, it is assumed that particles themselves are immobile and growth is the result of monomer transfer from particles smaller than a certain critical radius to particles larger than this radius. In the case of particle migration and coalescence, the particles are mobile, move across a support, and merge together upon interaction.

To understand and model sintering behavior and kinetics, most studies follow the behavior of an ensemble of particles. This is often done through the analysis of transmission electron microscopy (TEM)-derived average particle sizes and particle size distributions (PSDs) prior to and after sintering, resulting in several models. In the case of Ostwald ripening, sintering is usually described using the Lifshitz–Slyozov–Wagner (LSW) model, which predicts that the PSD is self-similar (the shape does not change with time) with a long tail toward smaller particle sizes, while the volume average particle size increases linearly with time.[5−7] For particle migration and coalescence, the process is usually described by some form of the Von Smoluchowski coagulation model, where the PSD displays a tail toward larger particles and typically fits a lognormal distribution.[8,9]

However, using PSDs before and after catalyst sintering often led to discrepancies between model predictions and experimental data. This is particularly noticeable in the case of Ostwald ripening, where the predicted small nanoparticles are almost never found in practice, and the reason why this was the case is unclear.[10] After OR, this then also results in a PSD that fits a lognormal distribution, which makes it impossible to infer the sintering mechanism from the PSDs alone.

A leap forward in solving these challenges has been made with the introduction of environmental TEM (ETEM), which

Received: October 31, 2019
Revised: December 23, 2019
Published: December 31, 2019

https://dx.doi.org/10.1021/acs.jpcc.9b10237
J. Phys. Chem. C 2020, 124, 2202–2212

allows direct in situ observation of catalyst nanoparticle sintering in a gas phase and at elevated temperature.[11−14] However, ETEM limits the studies of catalyst sintering processes to only those that take place in a gaseous environment and has a limited range of gas partial pressure (typically <5 mbar) due to the high vacuum requirements.[15] More recent developments in microfabrication allowed for cell-type holders and resulted in a wider range of gas pressures and gas types becoming available for in situ TEM.[16] However, these technologies still do not allow study of liquid phase sintering, which is a major issue in important systems such as catalysts for (H_2) polymer-electrolyte membrane fuel cells[17,18] or several biomass-to-chemical processes.[19−21]

It is not until recently that TEM imaging can also be performed in a liquid environment.[22−24] The so-called liquid-phase transmission electron microscopy (LP-TEM) is a powerful tool that allows visualization of materials in a liquid at a nanometer scale and has been, so far, successfully employed in studying, e.g., biomineralization,[25] protein movement over a cell membrane,[26] metal nucleation and growth,[27,28] electrochemical deposition and growth,[24,29] and oxide stability.[30−33] LP-TEM has also been used by Hermannsdörfer et al. to study the chemical stability of gold colloids in different aqueous environments.[34] In addition, Woehl et al. followed the aggregation of silver particles in situ.[35] These studies, although performed on unsupported and relatively large particles, do indicate that LP-TEM can have a great potential for studying catalyst sintering processes taking place in a liquid.

Studying sintering behavior in a liquid phase is particularly important for Au-based catalysts, highly attractive catalysts for a variety of industrial applications[36] such as the conversion of biomass to platform chemicals, which often takes place in a harsh aqueous environment.[19,21,37,38] Even when immobilized on a support, small gold nanoparticles invariably sinter rapidly in a liquid phase, especially in the presence of chloride ions, a common contaminant in biomass-derived feedstock.[39,40] This yields a lower specific surface area (SSA) and hence lower activity of the catalyst over time. Despite extensive work on the characterization of gold catalysts, our understanding of the processes underlying this sintering is limited.[36]

This work therefore employs the LP-TEM technique for the first time to study sintering of a titania-supported gold catalyst in a liquid environment. LP-TEM provided direct evidence that for gold nanoparticles of 3 nm number-average diameter Ostwald ripening is the main sintering mechanism, as predicted in a number of earlier studies; however, it also revealed that there is only a limited particle size dependence, as opposed to predictions and assumptions of the classical Ostwald ripening model.[41,42] Furthermore, it appears that this shrinkage is likely an activated process in which particles of all sizes investigated (1−5 nm) may shrink rapidly once destabilized. Particle growth, probably via monomer reattachment on the other hand, was slow and likely the rate-limiting step, while a significant fraction of particles did not change size at all. In the presence of large (∼20 nm) gold particles, the growth of ∼3 nm particles does not occur, but a similar fraction of particles still disappears and the mobile gold species are deposited on the large particles.

METHODS

Catalyst Synthesis. The gold−ethylene diamine complex salt $Au(H_2N{-}C_2H_4{-}NH_2)_2Cl_3$ was prepared following a modified method of Block and Bailar.[43] In a typical synthesis, 0.25 g of $HAuCl_4{\cdot}3H_2O$ (≥99.9%, Sigma-Aldrich) was dissolved in 2.5 mL of demineralized water in a glass beaker, while stirring the liquid at 400 rpm. After 10 min of stirring, 0.15 mL of pure ethylene diamine was added dropwise to the solution. The solution was then left to react for another 30 min at room temperature while stirring, after which the gold complex was precipitated by adding 30 mL of ethanol (99.8%, Sigma-Aldrich). The suspension was subsequently left to settle overnight, after which the liquid was removed and the precursor was further dried under vacuum to remove the ethanol. The powder was finally redissolved in 50 mL of Milli-Q water, resulting in a 11 mmol/L solution of $Au(H_2N{-}C_2H_4{-}NH_2)_2Cl_3$ in H_2O.

A 1 wt % gold supported on a titania catalyst with unimodal Au particle size distribution (3 nm number-average diameter) was prepared adapting the procedure of Zhu et al.[44] In a typical synthesis, 12 mL of the prepared 11 mmol/L solution of $Au(H_2N{-}C_2H_4{-}NH_2)_2Cl_3$ in H_2O was added to 18 mL of Milli-Q water, followed by addition of 0.5 mL of a 1.0 mol/L solution of NaOH (99%, Sigma-Aldrich) in Milli-Q water. After 5 min of vigorous stirring at 700 rpm, 3 g of commercial fumed TiO_2 powder (P25, Evonik Degussa) was dispersed in the solution while stirring. The dispersion was then left for 2 h at room temperature for the ionic gold precursor to adsorb on the TiO_2 surface. The solid was subsequently separated by centrifugation (10 min, 4000 rpm) and washed with 30 mL of demineralized water thrice.

The resulting powder was then dried overnight in an oven at 60 °C, followed by 24 h of vacuum-drying at room temperature. The resulting powder was subsequently heated in a fluidized bed reactor for 2 h at 300 °C in N_2, followed by 2 h at 400 °C in $20\%O_2/80\%N_2$, using a flow of 150 mL/min and a heating and cooling rate of 5 °C/min to reduce gold and remove the remaining ligands.

The bimodal sample was prepared by taking a part of the previously prepared unimodal sample followed by addition of a Au colloidal dispersion using the following procedure: 0.1 g of the original unimodal sample was dispersed in 10 mL of demineralized H_2O while stirring at 400 rpm. To this suspension, 3 μL of a 1.0 mol/L HNO_3 in H_2O solution was added, followed by addition of 2 mL of a commercial citrate-stabilized colloidal suspension of 20 nm gold nanoparticles (53 mg Au/L, 99% reactant free, Cytodiagnostics) for an additional colloid loading of maximum 0.1 wt % (resulting in a 1.1 wt % total gold loading on a titania catalyst).

After stirring for 2 h at 400 rpm, the solid was separated from the suspension by centrifugation (5 min, 4000 rpm), followed by washing thrice with 10 mL of demineralized water to remove the remaining ligands. The solid was subsequently dried overnight in an oven at 60 °C, followed by drying in vacuum for 24 h to obtain a powder.

In all of the synthesis steps, care was taken to limit the exposure of the gold (precursor) and catalyst to light as much as possible by covering the glassware with parafilm and aluminum foil to prevent light-induced reduction of gold ions. Care was also taken to prevent any contact of gold with metal by using poly(tetrafluoroethylene) (PTFE) and glass equipment.

Characterization. All samples were characterized by powder X-ray diffraction (XRD) using a Bruker D2 Phaser with a Co $K\alpha_1$ source for phase identification. Samples were evaluated for 2θ between 25 and 90°.

https://dx.doi.org/10.1021/acs.jpcc.9b10237
J. Phys. Chem. C 2020, 124, 2202−2212

N_2 physisorption measurements were performed at −196 °C (77 K) using a Micromeritics TriStar 3000 instrument. Before the isotherm measurements, samples were dried at 250 °C in air. Specific surface areas were calculated using the multipoint Brunauer−Emmett−Teller (BET) method ($0.05 < P/P_0 < 0.25$).

Catalyst morphology, gold particle size, and particle dispersion were examined with TEM using a Talos F200X (Thermo Fischer Scientific), operated at 200 kV acceleration voltage in both TEM and high-angle annular dark-field (HAADF)-scanning transmission electron microscopy (STEM) modes. The samples were dispersed in isopropanol (Honeywell, Chromasolv, 99.9%) and deposited on a 200 mesh copper-formvar grid. Gold particle sizes were subsequently determined by counting at least 250 particles manually using ImageJ.

Vacuum control experiments were performed by continuous STEM scanning for 1 h using a beam current of 0.21 nA, as determined by the electron current reaching the fluorescent screen without a holder present. For the control experiments in vacuum, imaging was performed using only the HAADF detector and at a magnification of 225k×, corresponding to a 500 × 500 nm^2 image size, resulting in an average dose rate of 5.2×10^3 $e^-/(nm^2 \cdot s)$. Images were collected with a pixel dwell time of 2.4 μs, with 2048 × 2048 pixel images, and for a total of 10 s/frame.

Ex situ sintering experiments were performed using a glass beaker with either 20 mL of Milli-Q water or 2 mL of a 0.1 mol/L NaCl in H_2O solution added to 18 mL of Milli-Q water. The liquid was subsequently stirred and heated to 80 °C while in contact with air. When the liquid temperature reached 80 °C, as measured by a stainless steel thermocouple in a separate vial of water to prevent any contact between gold and stainless steel, 30−50 mg of the catalyst was added and the glass beaker was covered with parafilm to prevent evaporation. A drop of the suspension was deposited on a TEM grid at regular time intervals (30 min, 1 h, 1.5 h, 2 h, 3 h, 4 h, 6 h, 8 h, 24 h) to be analyzed in TEM. In the case of the sintering experiment under N_2, a round-bottom flask in an oil bath and connected to a N_2 gas supply was used instead. N_2 was then bubbled through the solution starting 10 min before heating.

LP-TEM Experiments. *Liquid Cell Preparation.* A small and a large silicon chip with a nominally 50 nm thick silicon nitride (Si_xN_y) window of 20 × 550 μm^2 (Protochips Inc.) were cleaned in acetone and methanol according to manufacturer instructions. Subsequently, both the large and small chips were plasma-cleaned in an 80%Ar/20%O_2 plasma for 2 min to render the chip surface hydrophilic.

A small amount of either the unimodal or bimodal Au on the TiO_2 catalyst was then dispersed in 2 mL of high-purity isopropanol (Honeywell, Chromasolv, 99.9%) and sonicated for at least 15 min to disperse agglomerates. A 0.5 μL droplet of this suspension was placed on the silicon nitride layer of the large silicon liquid cell chip and left to dry for 5 min. This resulted in a sufficient amount of catalyst particles being attached to the window of a chip and thus available for imaging.

A small silicon chip, also containing a 20 × 550 μm^2 Si_xN_y window and 150 nm gold spacers to separate the two chips, was then placed in the dedicated liquid cell TEM holder (Protochips Inc.), a 1 μL drop of water (sterile-filtered, Bioreagent, ≤1 Eu/mL, ≤5 ppm metal impurities, Sigma-Aldrich) was added on top of it, and the cell was subsequently assembled by placing the large silicon chip containing the sample on top. In this configuration, the sample was dispersed on the top chip when the holder was inserted in the microscope for optimal spatial resolution in STEM mode.[22]

Imaging. Imaging was performed using Talos F200X (Thermo Fischer Scientific), operated in scanning transmission electron microscopy (STEM) mode at 200 kV acceleration voltage and using both a bright-field (BF) and a high-angle annular dark-field (HAADF) detector for imaging. The imaging was performed with a beam current of 0.21 nA, as determined by the screen current without a holder present in the electron microscope and with a camera length of 125 mm. Images were collected with a pixel dwell time of 2.4 μs, with 2048 × 2048 pixel images, and for a total of 10 s/frame. Experiments were performed at a magnification of 225k×, corresponding to a field of view of 500 × 500 nm^2, which results in an electron dose rate of 5.2×10^3 $e^-/(nm^2 \cdot s)$.

Each liquid cell experiment was performed in flow mode using a flow of 4 μL/min to prevent the buildup of gases and bubble formation due to electron-beam-induced water decomposition. Before an in situ experiment was started, either the H_2O or the 10 mmol/L NaCl solution was flushed through the holder for at least 30 min to ensure the liquid around the sample had the desired composition. In each experiment, the sample was continuously imaged in scanning (S)TEM mode with a total of 360 images being acquired, corresponding to exactly 1 h of electron beam scanning. The 10 mmol/L NaCl solution was prepared diluting a 100 mmol/L solution by adding 2 g of the latter to 18 g of ultrapure water. The 100 mmol/L solution was in turn prepared by dissolving 95 mg of NaCl (>99%, AkzoNobel) in 15 g of ultrapure H_2O in a clean glass vial.

Data Processing. Particle size was determined manually in all experiments using ImageJ software. For the ex situ experiments, the particle diameter was measured from HAADF-STEM images at 640k× magnification (image size of 175 × 175 nm^2). For the in situ measurements, images were first processed to enhance particle visibility using a Gaussian blur filter with a sigma of 1.5, followed by using the Despeckle function from ImageJ, which replaces each pixel with the median value of the 3 × 3 grid of pixels around it. Then, the images were aligned using the "linear stack alignment with SIFT" plugin. Ellipses were subsequently fitted manually to the particle projections in the BF-STEM images taken at 225k× magnification (500 × 500 nm^2 image size), from which the particle diameter was calculated. Particles were measured every 10th image, corresponding to every 100 s. When a particle was close to disappearing (typically from 1 min before disappearance but earlier if significant changes could be observed before), the size of that particle was measured every image until disappearance, corresponding to a measurement every 10 s. Further calculations of particle area and volume were performed assuming spherical particles. Particle size distributions were calculated from the diameter using a bin size of 1 nm, and the accompanying lognormal fit was calculated using the lognfit function in Matlab. The average diameters reported are all number-average diameters, calculated by summing all measured diameters and dividing by the number of particles.

Particles were classified as growing, shrinking, or remaining the same size by analyzing their size over time. Any particle that disappeared during the 1 h experiment was classified as shrinking, as no particles were found that decreased significantly in size (defined as getting smaller than 66.7% of

https://dx.doi.org/10.1021/acs.jpcc.9b10237
J. Phys. Chem. C 2020, 124, 2202−2212

the initial diameter) without disappearing. Particles that increased in diameter more than 33% of their initial diameter were classified as growing, while the other particles were deemed not to change size to any significant extent.

Specific surface area (SSA) was calculated from the particle size distribution by calculating the surface area and volume of each individual particle from its diameter, assuming spherical particles. These values were subsequently summed over all measured particles to obtain the total particle surface area and the total particle volume. Assuming the nanoparticles to have the density of bulk gold (19.3 g/cm^3), the total mass of all particles was calculated from their total volume and then the total surface area was divided by this total mass to obtain the specific surface area in m^2/g.

Fitting of the decrease in SSA was performed using the experimentally determined third-order power law for the rate of decrease of specific surface area (eq 1), in which a is the specific surface area normalized with respect to the initial specific surface area (on a scale from 0 to 1), t is the time in min, and k is the rate constant

$$\frac{da}{dt} = -ka^3 \tag{1}$$

Solving this differential equation results in the description of a as a function of t, as shown in eq 2

$$a = \sqrt{\frac{1}{\left(C + \frac{1}{2}kt\right)}} \tag{2}$$

in which C is the constant of integration. Assuming a to be 1 for t = 0 (in other words, assuming that the specific surface area is equal to the initial specific surface area when t = 0), this results in C being equal to 1. The rate constant k was subsequently determined by fitting the measured data points using the least-squares method in Matlab.

RESULTS AND DISCUSSION

Au/TiO$_2$ Catalysts. To study the liquid phase growth of gold nanoparticles supported on TiO$_2$, two samples were prepared, one with a unimodal and one with a bimodal particle size distribution (PSD). The unimodal Au/TiO$_2$ catalyst sample was synthesized using a gold−ethylene diamine complex and titanium dioxide nanopowder (P25, Evonik) by adapting the procedure of Zhu et al.[44] The bimodal Au/TiO$_2$ sample was prepared by depositing 20 nm gold colloidal particles on the previously prepared unimodal Au/TiO$_2$ sample, resulting in the desired bimodal particle size distribution.

Scanning transmission electron microscopy (STEM) images showed that Au nanoparticles with a number-average diameter of 3 nm, relatively narrow size distribution, and uniform distribution across the TiO$_2$ support were present in both the unimodal (Figure 1a,b) and bimodal (Figure 1c,d) samples. Next to 3 nm Au particles, the bimodal sample also contained well-dispersed 20 nm colloidal Au particles (Figure 1d). X-ray diffraction and N$_2$ physisorption analyses of the pristine TiO$_2$ support and the unimodal catalyst (Figure S1) indicated that the TiO$_2$ support structure of the unimodal sample was not altered during gold deposition. The TiO$_2$ powder still consisted of a mixture of anatase and rutile crystallites in the same ratio and the BET specific surface area remained 45 m^2/g. Gold loading was 0.9 wt % for the unimodal sample, as

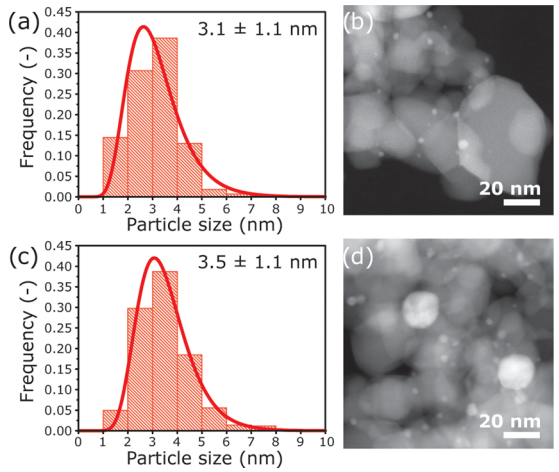

Figure 1. Particle size distributions (PSDs) with a lognormal fit and representative high-angle annular dark-field scanning transmission electron microscopy (HAADF-STEM) images of the unimodal (a, b) and the bimodal (c, d) Au/TiO$_2$ samples, respectively. Only the small particles (<10 nm) are included in the PSD of the bimodal sample.

determined by inductively coupled plasma atomic emission spectrometry (ICP-AES).

Sintering Behavior of the Unimodal Sample. Sintering of the individual Au nanoparticles in a liquid environment was investigated in situ using a specialized liquid-phase (LP) TEM holder (Poseidon Select, Protochips Inc.). This system consists of two chips with electron-transparent Si$_x$N$_y$ windows, between which a thin layer of liquid and the sample are sandwiched to allow imaging while keeping the liquid separate from the high vacuum inside the TEM column, as illustrated in Figure S2. Using this system, it was possible to observe sintering behavior directly at the nanoscale with high spatial and temporal resolution.

Considering the inertness of gold in an aerated aqueous environment, no or limited sintering and other structural changes would be expected in the presence of water and dissolved oxygen alone.[45] However, the presence of chloride ions is detrimental to the stability of gold nanoparticles. It promotes sintering, both in gas and liquid phases and/or when present on the support, due to the ability of chloride to form a complex with gold ions, which results in the stabilization of mobile ionic gold species.[46,47] Therefore, sintering was investigated with LP-TEM in both water and a 10 mmol/L solution of NaCl. In addition to these in situ experiments, ex situ laboratory studies were performed to ensure that in situ observations accurately represent the actual sintering behavior in this system. For ex situ studies, 30−50 mg of catalyst was exposed to the same water or 10 mmol/L NaCl in water environment used in situ, and the dispersion was heated to 80 °C to accelerate sintering.

Figure 2a,b displays the resulting PSDs of the unimodal sample based on 200−300 particles at different times in an NaCl environment for the in situ and ex situ experiments, respectively. Furthermore, a representative STEM image associated with each moment in time, for which the PSD was determined, is displayed as well, along with Movie M2 showing the real-time nanoparticle behavior during an entire in situ experiment. As can also be observed in Figure 2, the liquid layer limits the attainable resolution in LP-TEM to an extent and bright-field (BF) STEM imaging mode has been found to yield better resolution and contrast compared to high-angle

https://dx.doi.org/10.1021/acs.jpcc.9b10237
J. Phys. Chem. C 2020, 124, 2202−2212

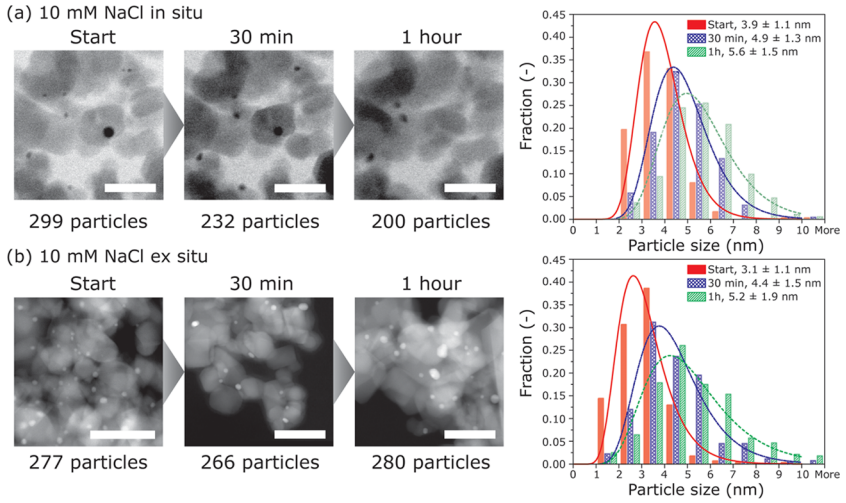

Figure 2. In situ and ex situ (a and b, respectively) comparison of the evolution of the particle size distributions for the Au/TiO_2 sample with unimodal particle size distribution in a 10 mmol/L NaCl aqueous solution. A representative scanning transmission electron microscopy image in a bright-field (BF) (a) or a high-angle annular dark-field (HAADF) (b) mode is shown for three different times, corresponding to the particle size distributions displayed in the graph on the right side of the images. For in situ experiments, images were taken at the same position. The scale bar in each image corresponds to 50 nm.

annular dark-field (HAADF) STEM.[48] For imaging thin samples in vacuum (the ex situ samples) on the other hand, HAADF-STEM showed better contrast.

In both the in situ and ex situ experiments, growth of the Au nanoparticles in NaCl was observed after 1 h. In situ LP-TEM unambiguously showed that particle growth proceeded through Ostwald ripening, where particles did hardly move but changed in size, most likely through monomer transfer via the liquid phase. Particle migration and coalescence, as the other possible sintering mechanism, could be excluded noting that only two merging events within several hundred particles were observed and, overall, Au particles displayed a very low mobility on the TiO_2 surface. The presence of NaCl was shown to be crucial for sintering, since in both the in situ and ex situ experiments in water, very limited growth of Au particles was observed (Figure S3 and Movie M1).

To exclude the possibility of primary damage by the electron beam influencing the observed particle growth, the samples were exposed to the same electron beam treatment in the vacuum of the electron microscope (Figure S4). No sintering or other alteration of the catalyst was observed, which confirms that the presence of a liquid medium was crucial for sintering. The support was not affected in the experiments, as the LP-TEM experiments with the pristine P25 TiO_2 in H_2O or a 10 mmol/L NaCl solution under the same imaging conditions showed no changes of the TiO_2 structure (Figure S5).

It was found however that the sintering rate did depend on the NaCl concentration. This is illustrated in Figure S6, where two in situ experiments in a solution of 10 and 100 mmol/L NaCl in H_2O are compared, with sintering being significantly faster in the latter. As 10 mmol/L NaCl yielded a more suitable time scale to observe sintering, this concentration was used throughout further experiments.

Importantly, PSDs derived from the in situ experiments in 10 mmol/L NaCl (Figure 2a) do display the self-similar evolution characteristic for Ostwald ripening. However, they also show a tail toward the right, which is in disagreement with classical OR models and more akin to migration and coalescence. The evolution of the PSD does however correspond well to Ostwald ripening behavior observed in practice.[5,6] Clearly, direct in situ observation was crucial to determine the growth mechanism, as PSD analysis before and after growth could have led to the incorrect conclusion that this is either a mix of two mechanisms or even migration and coalescence only.

Furthermore, the PSDs derived from the in situ experiments are in good agreement with the PSDs obtained from the laboratory ex situ experiments (Figure 2b), although the beam did accelerate sintering somewhat. Because of this, in situ sintering experiments were performed at room temperature while ex situ the sample was heated to 80 °C to accelerate particle growth to similar time scales. The acceleration during the in situ LP-TEM measurements likely originates from the oxidizing $^{\bullet}OH$ radical and H_2O_2 and reducing hydrated electron ($e_{(aq)}^-$) produced by the beam, as it has been observed before that these radicals are able to accelerate growth of gold colloids.[34] Particle size measurements of nanoparticles well outside the reach of the radicals (>5 × 0.2 μm^2, the latter of which is the Fick diffusion length in water for the lifetime of these radicals) were also performed after an in situ experiment. These particles were found to have the same PSD as the initial PSD of the irradiated area, confirming that the electron beam was indeed accelerating sintering somewhat but that the overall beam effects were minor.

However, to ensure that our in situ observations were indeed representative for ex situ behavior, an additional control experiment was performed using liquid cell heating chips to perform an in situ experiment at 80 °C in the presence of 10 mmol/L NaCl in H_2O. Due to the electron beam and heating combination resulting in significant acceleration of growth, imaging of the region of interest was performed every 5 min, with the beam being blanked in between. Even then, significant acceleration of sintering compared to only heating or only using the electron beam was observed. Nevertheless, as can be observed in Figure S8, the behavior was qualitatively similar to both the in situ and ex situ observations and the rate was quite similar to that in the in situ experiment at room temperature with 100 mmol/L NaCl.

https://dx.doi.org/10.1021/acs.jpcc.9b10237
J. Phys. Chem. C 2020, 124, 2202−2212

Individual Au Nanoparticle Study. Although the behavior of the assembly of particles seems to match Ostwald ripening observations for catalysts very well,[10] LP-TEM revealed that the dynamic behavior of individual nanoparticles is remarkably different from expectations. This is illustrated in Figure 3, wherein the size evolution of several individual particles over time is displayed. In most Ostwald ripening models, it is assumed that larger particles will grow at the expense of smaller particles, as a result of the higher specific surface energy of particles with a more convex surface. Models then typically predict a time-dependent critical particle diameter d, where particles smaller than d shrink, while all particles with a diameter larger than d are expected to grow.[49]

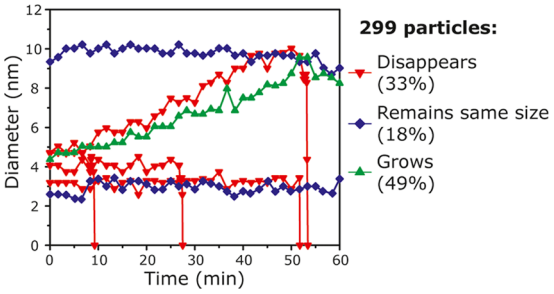

Figure 3. Diameter evolution over time of several particles during the in situ study of unimodal Au/TiO_2 in a solution of 10 mmol/L NaCl in H_2O. Different evolution paths were observed, including shrinking/disappearing particles (solid, red inverted triangle), particles that remain approximately the same size (solid, blue diamond), and particles that grow (solid, green upright triangle), with the percentage of particles displaying each type of behavior shown in the legend.

Strikingly, Figure 3 and Movie M2 actually reveal that the size of a nanoparticle does not seem to have a large influence on the type of behavior it displays. In our experiments, many of the larger (3−5 nm) particles were also found to shrink, while part of the smaller (1−3 nm) particles were seen to grow (Movie M2) and particles of all sizes could remain stable. The limited effect of particle size on the probability that it disappeared is also illustrated in Figure 4. Here, each point corresponds to the diameter of an individual particle at the moment it starts disappearing along with the time at which it disappears and the solid line showing the number-average particle size over time. This figure highlights that although the majority of particles disappearing have a size below average, there is also a significant fraction above average size.

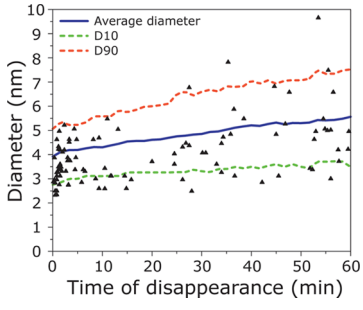

Figure 4. Overview of the diameter of each measured particle at the moment it starts disappearing, along with the corresponding time of disappearance for the in situ experiment in 10 mmol/L NaCl dissolved in H_2O. Each point in the graph corresponds to a single particle. The solid line corresponds to the number-average particle diameter, and the lower and upper dashed lines correspond to D10 and D90, the size below which 10 and 90% of the particle population lies, respectively.

Besides an indifference to size, in situ data related to Figure 3 also revealed that although nanoparticles grew slowly over time, nanoparticle shrinkage was a fast process. From Movie 2 and Figure S7, in which a few consecutive frames of a disappearing nanoparticle are displayed, it is also clear that nanoparticles did not detach from the support, as they remained spherical and attached to TiO_2. This, combined with the lack of nanoparticle mobility observed and the absence of reattaching/appearing nanoparticles, suggests that they dissolve as monomeric ionic gold species in line with an Ostwald ripening mechanism. This fast disappearance could also cause discrepancies between the LSW model predictions, which predict an asymmetric PSD skewed to smaller particles, and experimentally determined PSDs, where these smaller particles are almost never observed. These results indicate that nanoparticles in this size range disappear too fast to be observed at any given time.

Another important observation is that a meaningful fraction of approximately 18% of nanoparticles does not seem to change size to any significant extent, while models predict nanoparticles to either grow or shrink.

To understand the origin of the fast disappearance and limited influence of particle size, it is helpful to first consider the thermodynamic properties of this system. As previously mentioned, the formation of mobile Au^{3+} species from metallic gold under standard conditions is highly unfavorable, but the addition of chloride ions results in the formation of an $[AuCl_4]^-$ complex, which has a significantly lower reduction potential[50]

$$Au^{3+} + 3e^- \rightleftharpoons Au; \quad E^0 = 1.50\ V$$

$$[AuCl_4]^- + 3e^- \rightleftharpoons Au + 4Cl^-; \quad E^0 = 1.00\ V$$

$$O_2 + 4H^+ + 4e^- \rightleftharpoons 2H_2O; \quad E^0 = 1.229\ V$$

As these are standard potentials, low gold ion concentrations and high concentrations of oxygen, chloride ions, and hydronium ions have to be present for the oxidation of gold to be thermodynamically favorable. In the conditions used in this work (pH = 7, P_{O_2} = 0.2 bar), the reduction potential of reaction 3 is only 0.81 V though, indicating that the chemical equilibrium should still be toward bulk metallic gold. Although theoretical calculations indicate that water irradiated with electrons has a small drop in pH to approximately 4.5 within the irradiated area for the irradiation conditions used in this work,[45] this pH would still have an equilibrium toward bulk metallic gold. However, it is well known that the reduction potential of gold ions rapidly decreases with gold particle size, especially for nanoparticles smaller than approximately 10 nm, as a result of the higher fraction of low-coordinated surface atoms present.[41,51] Work by Ivanova et al.[52] indicates that this shift can be in excess of 0.2 V for ∼4 nm particles, which indicates that dissolution can actually be favorable for all particles present in these samples when the concentration of chloride ions is sufficiently high.

Some calculations on the equilibrium concentrations of the $[AuCl_4]^-$ complex for different pH values, Cl^- concentrations, and O_2 partial pressures are listed in Table S1. These values indicate that concentrations of the complex are low but significant for particles in this size range. The previously

https://dx.doi.org/10.1021/acs.jpcc.9b10237
J. Phys. Chem. C 2020, 124, 2202−2212

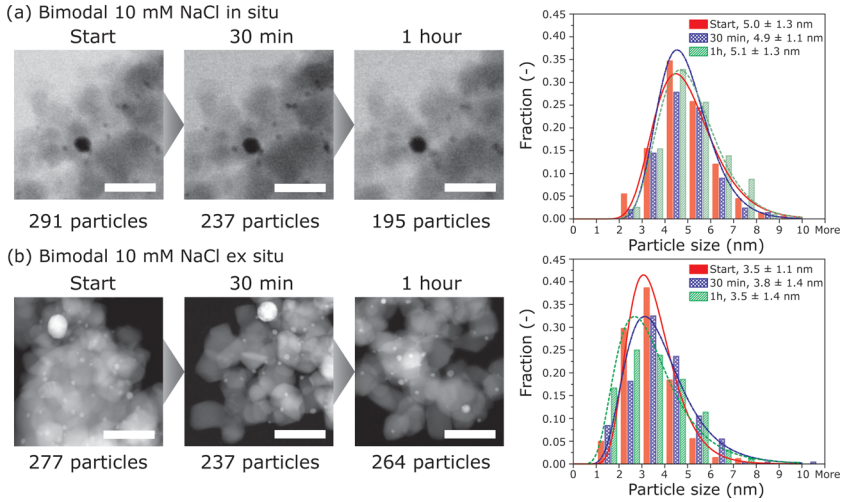

Figure 5. In situ and ex situ (a and b, respectively) comparison of the evolution of the particle size distributions for the small particles (<10 nm) of the Au/TiO_2 sample with bimodal particle size distribution in a 10 mmol/L NaCl in water solution. Due to the limited number of large particles (20 nm) and the uncertainty in the bulk ratio of smaller to larger particles, the large particles were not included in these PSDs. A representative scanning transmission electron microscopy image in bright-field (BF) (a) or high-angle annular dark-field (HAADF) (b) mode is shown for three different times, corresponding to the particle size distributions displayed in the graph on the right side of the images. For the in situ experiments, each image is taken at the same position. The scale bar in each image corresponds to 50 nm.

mentioned in situ experiment with 100 mmol/L NaCl in H_2O (Figure S6) also demonstrates that the concentration of chloride ions is indeed important. Additionally, to investigate the influence of oxygen on Ostwald ripening, we have also performed a laboratory sintering experiment in a 10 mmol/L NaCl solution under an inert N_2 atmosphere instead of air. The results presented in Figure S9 clearly showed that the absence of O_2 significantly slowed down sintering, indicating that oxidation of gold by oxygen is crucial and $[AuCl_4]^-$ complexes are likely the mobile species.

Next to these thermodynamic aspects, we expect that the rate of the oxidation process is affected by kinetics too. It is likely that this dissolution occurs preferentially at defects/low-coordinated Au atoms and is able to proceed rapidly once such a site is available in a nanoparticle through thermal fluctuations in the experiments. It has been shown previously that such single events can indeed destabilize small silver nanoparticles and likely explain the observed rapid dissolution observed in these experiments.[53,54] This would also explain why particles of all sizes are dissolving, although with a bias toward smaller particles. The preference for smaller particles is likely a combination of their being more prone to oxidation (thermodynamics) and the faster formation of defects (kinetics), increasing their changes of being destabilized.

The slow growth of particles of all sizes indicates that reattachment of gold monomers to particles is a kinetically limited process and likely requires sites of high coordination for attaching gold atoms. This suggests that thermodynamic constraints are not prevailing once particles start growing and that growth requires a surface configuration containing such high coordination sites. In addition, Figure 3 shows a delay of roughly 10 min before particle growth started, and according to Figure 4, significantly more particles disappeared during those first 10 min, indicating that a certain concentration of the $[AuCl_4]^-$ complex is necessary before growth proceeds at measurable rates.

Another possible explanation that should be considered is that the surface of gold is not always completely accessible as a result of ligand coverage. However, the synthesis procedure includes a high-temperature calcination step that should be sufficient to remove all of the remaining ethylene diamine ligands and any other organic contamination. It is therefore likely that almost all of the gold nanoparticles are completely accessible. The limited divergence in nanoparticle shape, also at the interface with the TiO_2 support, indicates that the interaction of gold with the TiO_2 support is very similar for all particles. Consequently, we expect that local differences in nanoparticle surface chemistry and accessibility do not play a significant role in the differences observed between the individual nanoparticles in these Ostwald ripening experiments.

The previously mentioned kinetic limitations might also explain why a significant fraction of particles do not change size during the experiments. Certain gold−support interactions or facets being exposed might result in slower kinetics for either gold oxidation or gold-ion reduction and attachment, resulting in very limited or no change in size. Although difficult to observe as a result of the small size, some facet formation during growth seems to take place for part of the particles. In the experiments with in situ heating with 10 mmol/L NaCl in water (Figure S8) and in the in situ experiments with 100 mmol/L NaCl at room temperature (Figure S6), several particles do have clear facets upon growth. The facet growth is likely more visible as a result of the larger final particle size obtained in these experiments. This facet formation during growth is another strong indication of reattachment taking place at specific surface structures.[28,55] It could also be argued that some of these particles are inside support pores and their size is limited by the pore size.[56] However, several particles that are clearly not inside a pore were also found to remain the same size, as illustrated in Figure S10, and therefore this explanation is not satisfactory for all particles.

Bimodal Au Particle Size Distribution. To study the effect of the presence of significantly larger particles on sintering, we also prepared a sample with a bimodal particle size distribution by depositing 20 nm Au colloids on the unimodal sample with ~3 nm Au particles. Due to their larger size, these particles should be significantly more stable and

https://dx.doi.org/10.1021/acs.jpcc.9b10237
J. Phys. Chem. C 2020, 124, 2202−2212

attachment kinetics should be more favorable.[52] When subjecting this sample to the same conditions as those used for the unimodal sample, in situ and ex situ experiments with only water present again showed only limited changes in Au particle size (Figure S11 and Movie M3).

In the presence of 10 mmol/L NaCl, the same fraction of small (1−5 nm) particles compared to the unimodal sample in NaCl disappeared in the same manner (33% in both cases), by shrinking and disappearing in less than 1 min. Although more stable than the small particles, the 20 nm particles are still significantly less stable than bulk gold and could therefore be expected to dissolve as well, albeit with lower probability.[52] It was indeed observed that one of the 21 observed large particles dissolved, which again indicates that dissolution is a stochastic process with only a limited influence of nanoparticle size for particles in this size range.

Surprisingly, although the same fraction of particles disappear, the remaining small (~3 nm) particles did not change in size significantly in both the in situ and ex situ experiments, as Figure 5 and Movie M4 demonstrate. The 20 nm particles seemed to grow somewhat, but due to their large volume, the change in diameter is much harder to accurately determine compared to small particles. Assuming conservation of gold in the field of view, the diameter of the large particles would increase by approximately 2 nm at most when all of the gold is deposited on these particles. In addition, the large size also results in a more gradual change in contrast at the edges of the particles, making it more difficult to exactly determine the diameter of the particle. An example of this measured size evolution of two of these larger particles is presented in Figure S12.

Still, the lack of growth of the small particles in the bimodal system suggests that $[AuCl_4]^-$ monomer reattachment is predominantly happening on the larger particles. It is therefore likely that monomer reattachment is rate-limiting for Ostwald ripening in this system, as the thermodynamic driving force is larger for gold reattachment on the larger particles.[52] Diffusion limitations are unlikely, as in the case of the in situ experiments, typical ion diffusion lengths (~30 μm for 1 s in water) are significantly larger than the area being irradiated by the electron beam used to drive sintering (0.5 μm × 0.5 μm). In the case of the ex situ experiments, vigorous stirring ensured a homogeneous dispersion of catalyst and fast mixing through convection. Furthermore, in the presence of diffusion limitations, one would generally expect the formation of at least some dendritic structures, whereas none were observed.[57]

Sintering Kinetics. For catalysis, the specific surface area (SSA) or the surface area per gram of the active material, in this case, the gold nanoparticles, is an important factor for the activity of the catalyst, as it determines the amount of active sites available to catalyze a chemical reaction. Using the obtained PSDs from the in situ experiments, this gold SSA was determined over time for the unimodal sample in 10 mmol/L NaCl and compared to the values obtained from the ex situ experiments acquired at 10 minute intervals. This comparison, presented in Figure 6, shows that this specific surface area decreases significantly over time, both in situ and ex situ, which would result in significant deactivation of the catalyst.

The rate of decrease in SSA through sintering is often fitted using a power-law fit, with an experimentally observed third-order dependence for Ostwald ripening.[1] Realizing the short time scale, fitting our in situ data with a third-order power law shows quite good agreement with the measured data for the in situ results. As can be observed, there is a large scatter in the ex situ results, as it was not possible to sample the same areas of the catalyst multiple times. This results in a larger error in the acquired particle size distribution and therefore a larger error in the rate constants obtained from short time experiments. Owing to this larger error, long-term, expensive catalyst sintering experiments are often required to accurately predict sintering behavior.[41] In situ observations could therefore aid significantly in building more accurate Ostwald ripening models and with great potential as a quantitative method for predicting long-term Ostwald ripening.

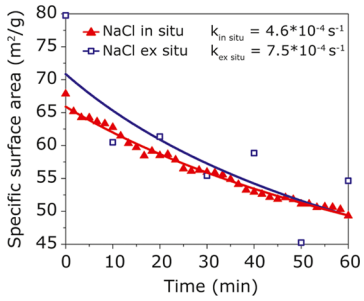

Figure 6. Gold specific surface area in m^2/g with measured values (symbols) and the fit (lines) for both the in situ and ex situ experiments on the unimodal sample in a solution of 10 mmol/L NaCl in H_2O.

The same kinetic analysis was performed for sintering of the sample with bimodal PSD as well, but as previously mentioned, it is challenging to observe the change in diameter of the large particles (~20 nm). As a result, the gold mass balance in the field of view is significantly harder to determine and therefore, so is the specific surface area. In addition, it is very difficult to obtain the same ratio of gold mass between small particles and large particles in the in situ experiments as compared to the bulk sample. In our case, approximately 30% of the gold mass consisted of large particles at the start of the in situ experiments, while in the bulk, this is ≤10%. Due to this, in our analysis, only the surface area of the small particles was taken into account, which does however correspond to >95% of the overall surface area in the bulk sample. It was assumed that the total volume of gold in the field of view was constant and that all of the gold from the disappeared particles was deposited on the large particles.

The result of this analysis for the decrease in SSA, normalized with respect to the initial SSA, is displayed in Figure 7, along with the normalized SSA of the unimodal sample. It can be seen that the gold SSA decreased faster for the bimodal sample than for the unimodal sample, although the difference becomes smaller after longer times. A likely explanation for this observation is that in the case of the unimodal sample the amount of gold in the field of view was found to increase with time, which yields a net faster decrease in SSA. This increase could partially result from the fact that some of the smallest particles could be hard to observe in the liquid cell, resulting in more gold present at the start than actually measured, but it is possible that some gold is transported into the field of view from the surrounding area in all experiments. When comparing the areas close to the imaged area before and after each experiment, it also seems that a few particles just outside of the irradiated area have disappeared, indicating that there is indeed some gold entering the field of view, as can be seen in Figure S13. This net

https://dx.doi.org/10.1021/acs.jpcc.9b10237
J. Phys. Chem. C 2020, 124, 2202−2212

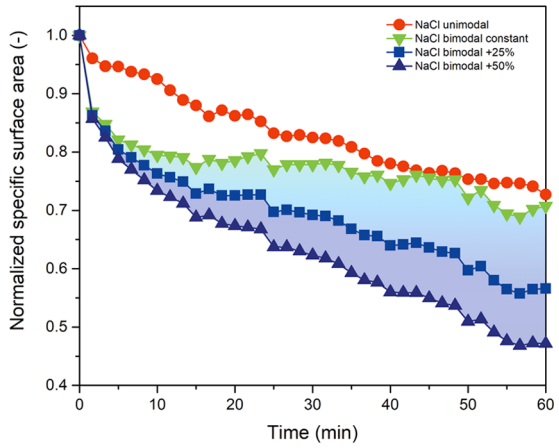

Figure 7. Gold specific surface area change over time derived from in situ experiments for the unimodal and bimodal sample in a solution of 10 mmol/L NaCl in H_2O, normalized with respect to the initial specific surface area. For the bimodal sample, three different lines are plotted, assuming an influx of gold in the field of view of 0, 25, and 50% of the initial amount of gold. The highlighted area in between indicates that the range of possible SSA decreases for the bimodal sample.

transport could be the result of the reducing radicals present in the field of view, which are a stronger and more reactive reducing agent than water. Reduction of the ionic gold complex in the field of view might then be slightly easier than outside of the field of view, resulting in a slightly lower gold concentration in the field of view and therefore net diffusive transport. It is however not possible to determine the exact amount of gold coming into the field of view for the in situ experiments with the bimodal sample.

However, when assuming that an amount of gold comparable to that in the unimodal in situ experiments is entering the field of view and also depositing on the large particles during the bimodal experiment, the SSA decreases a lot faster during the bimodal experiments and the fitted Ostwald ripening rate constant is significantly higher. This is illustrated by the shaded area in Figure 7, where it was assumed that an additional amount of gold entered the field of view ranging from 0 to 50% of the initial amount of gold. This 50% increase of gold represents the maximum increase found for all except one of the in situ experiments with the unimodal sample.

These results do however clearly show that the specific surface area decreases significantly faster in the sample with bimodal particle size distribution, despite the almost nonexistent growth of most particles. This can be explained by the fact that a very similar fraction (~33%) of particles disappears in both samples but that in the bimodal sample, gold mostly redeposits on the large particles, with a negligible contribution to the overall SSA. In the unimodal sample, gold redeposits on other small particles, which then still have a significant SSA to which the redeposited gold can contribute. Hence, almost no gold is incorporated in very large particles in the unimodal sample, resulting in a significantly slower decrease in SSA.

These observations also provide a good explanation for a puzzling phenomenon often observed in catalytic experiments. It is often seen that a catalyst with a few large clusters deactivates faster than a similar catalyst without those clusters as a result of a decreasing specific surface area. Surprisingly though, investigation of the deactivated catalyst usually shows that the individual particles in the catalyst with the large clusters have grown significantly less than in the other catalyst, and one would expect this catalyst to have a higher specific surface area and therefore a higher activity.[58] If a significant fraction of the particles disappears and the metal is incorporated in very large clusters with a negligible SSA, the overall SSA of the catalyst is significantly lower than when all particles grow just a little bit, which results in faster catalyst deactivation.

CONCLUSIONS

In conclusion, the present work offers new fundamental insights into the mechanism of Ostwald ripening of supported metal nanoparticles in a liquid phase and highlights the power of liquid-phase electron microscopy for investigating such processes in situ. An Au/TiO_2 catalyst was used as a case study and dissolved Cl^- ions as sintering promoters. We found that although the behavior of the ensemble of particles agrees well with previous work in the literature and our ex situ results, the nanoscale mechanisms differ significantly from expectations. Particle dissolution was sudden and seemed a stochastic process, while particle growth, that is, monomer attachment, was slow and likely the rate-determining step for sintering in this system. We also observed the existence of a significant fraction of inert particles that neither grew nor shrank. Furthermore, gold particle size has been shown to matter significantly less than predicted in classical Ostwald ripening models. Clearly, investigations of sintering processes at the individual nanoparticle level opposed to nanoparticle ensemble are instrumental for gaining new insights into the mechanisms involved and improving predictive power of sintering models.

ASSOCIATED CONTENT

Supporting Information

The Supporting Information is available free of charge at https://pubs.acs.org/doi/10.1021/acs.jpcc.9b10237.

Additional N_2 physisorption and XRD characterization data of the catalyst and support, detailed insets of a single particle (~8 nm initially) shrinking, a single particle outside a interparticle pore of the support not changing size, diameter evolution of two large gold particles of ~20 nm in the bimodal sample and an inset of the area outside of the scanned region; table listing equilibrium concentrations of the $[AuCl_4]^-$ complex under various conditions encountered in this work; several LP-TEM control experiments: behavior of unimodal and bimodal PSD samples in H_2O without NaCl in situ and ex situ, continuous STEM of the P25 TiO_2 support in H_2O with and without 10 mmol/L NaCl in situ, continuous STEM of the catalysts in vacuum, comparison of 10 mmol/L NaCl vs 100 mmol/L NaCl in situ, the heating LP-TEM experiment of the unimodal sample in situ, the ex situ experiment of the unimodal sample under a N_2 atmosphere in a solution of 10 mmol/L NaCl in H_2O (PDF)

Movie showing an experiment in H_2O for the unimodal PSD sample (Movie M1) (AVI)

Movie showing an experiment in 10 mmol/L NaCl solution for the unimodal PSD sample (Movie M2) (AVI)

https://dx.doi.org/10.1021/acs.jpcc.9b10237
J. Phys. Chem. C 2020, 124, 2202−2212

Movie showing an experiment in H_2O for the bimodal PSD sample (Movie M3) (AVI)

Movie showing an experiment in 10 mmol/L NaCl solution for the bimodal PSD sample (Movie M4) (AVI)

AUTHOR INFORMATION

Corresponding Authors

Krijn P. de Jong − *Utrecht University, Utrecht, The Netherlands*; orcid.org/0000-0002-9773-8110; Email: K.P.deJong@uu.nl

Jovana Zečević − *Utrecht University, Utrecht, The Netherlands*; Email: J.Zecevic@uu.nl

Other Author

Mark J. Meijerink − *Utrecht University, Utrecht, The Netherlands*

Complete contact information is available at: https://pubs.acs.org/10.1021/acs.jpcc.9b10237

Author Contributions

All authors contributed equally to this work.

Notes

The authors declare no competing financial interest.

ACKNOWLEDGMENTS

The authors acknowledge J.D. Meeldijk for technical assistance with the electron microscope, L. Weber for the N_2 physisorption measurements, and S.M.C. de Jong for help with the synthesis. K.P.d.J. and M.J.M. acknowledge funding from the European Research Council, EU FP7 ERC Advanced Grant no. 338846. J.Z. acknowledges financial support by Netherlands Organization for Scientific Research (NWO), Veni Grant no. 722.015.010.

ABBREVIATIONS

TEM, transmission electron microscopy; LP-TEM, liquid-phase (in situ) TEM; STEM, scanning transmission electron microscopy; HAADF-STEM, high-angle annular dark-field STEM; BF-STEM, bright-field STEM; PSD, particle size distribution; SSA, specific surface area

REFERENCES

(1) Prieto, G.; Zečević, J.; Friedrich, H.; De Jong, K. P.; De Jongh, P. E. Towards Stable Catalysts by Controlling Collective Properties of Supported Metal Nanoparticles. *Nat. Mater.* **2013**, *12*, 34−39.

(2) Farokhzad, O. C.; Langer, R. Impact of Nanotechnology on Drug Delivery. *ACS Nano* **2009**, *3*, 16−20.

(3) Valden, M.; Lai, X.; Goodman, D. W. Onset of Catalytic Activity of Gold Clusters on Titania with the Appearance of Nonmetallic Properties. *Science* **1998**, *281*, 1647−1650.

(4) Dai, Y.; Lu, P.; Cao, Z.; Campbell, C. T.; Xia, Y. The Physical Chemistry and Materials Science Behind Sinter-Resistant Catalysts. *Chem. Soc. Rev.* **2018**, *47*, 4314−4331.

(5) Lifshitz, I. M.; Slyozov, V. V. The Kinetics of Precipitation from Supersaturated Solid Solutions. *J. Phys. Chem. Solids* **1961**, *19*, 35−50.

(6) Wagner, C. Theorie Der Alterung Von Niederschlägen Durch Umlösen (Ostwald-Reifung). *Z. Elektrochem., Ber. Bunsen-Ges. Phys. Chem.* **1961**, *65*, 581−591.

(7) Kahlweit, M. Ostwald Ripening of Precipitates. *Adv. Colloid Interface Sci.* **1975**, *5*, 1−35.

(8) Von Smoluchowski, M. Drei Vortrage Uber Diffusion. Brownsche Bewegung Und Koagulation Von Kolloidteilchen. *Z. Phys.* **1916**, *17*, 557−585.

(9) Granqvist, C. G.; Buhrman, R. A. Size Distributions for Supported Metal Catalysts: Coalescence Growth Versus Ostwald Ripening. *J. Catal.* **1976**, *42*, 477−479.

(10) Datye, A. K.; Xu, Q.; Kharas, K. C.; McCarty, J. M. Particle Size Distributions in Heterogeneous Catalysts: What Do They Tell Us About the Sintering Mechanism? *Catal. Today* **2006**, *111*, 59−67.

(11) Challa, S. R.; Delariva, A. T.; Hansen, T. W.; Helveg, S.; Sehested, J.; Hansen, P. L.; Garzon, F.; Datye, A. K. Relating Rates of Catalyst Sintering to the Disappearance of Individual Nanoparticles During Ostwald Ripening. *J. Am. Chem. Soc.* **2011**, *133*, 20672−20675.

(12) Liu, R.-J.; Crozier, P. A.; Smith, C. M.; Hucul, D. A.; Blackson, J.; Salaita, G. Metal Sintering Mechanisms and Regeneration of Palladium/Alumina Hydrogenation Catalysts. *Appl. Catal., A* **2005**, *282*, 111−121.

(13) Simonsen, S. B.; Chorkendorff, I.; Dahl, S.; Skoglundh, M.; Sehested, J.; Helveg, S. Direct Observations of Oxygen-Induced Platinum Nanoparticle Ripening Studied by in Situ TEM. *J. Am. Chem. Soc.* **2010**, *132*, 7968−7975.

(14) Van den Berg, R.; Elkjaer, C. F.; Gommes, C. J.; Chorkendorff, I.; Sehested, J.; De Jongh, P. E.; De Jong, K. P.; Helveg, S. Revealing the Formation of Copper Nanoparticles from a Homogeneous Solid Precursor by Electron Microscopy. *J. Am. Chem. Soc.* **2016**, *138*, 3433−3442.

(15) Hansen, T. W.; Wagner, J. B.; Hansen, P. L.; Dahl, S.; Topsøe, H.; Jacobsen, C. J. H. Atomic-Resolution in Situ Transmission Electron Microscopy of a Promoter of a Heterogeneous Catalyst. *Science* **2001**, *294*, 1508−1510.

(16) Kawasaki, T.; Ueda, K.; Ichihashi, M.; Tanji, T. Improvement of Windowed Type Environmental-Cell Transmission Electron Microscope for in Situ Observation of Gas-Solid Interactions. *Rev. Sci. Instrum.* **2009**, *80*, No. 113701.

(17) Borup, R.; Meyers, J.; Pivovar, B.; Kim, Y. S.; Mukundan, R.; Garland, N.; Myers, D.; Wilson, M.; Garzon, F.; Wood, D.; et al. Scientific Aspects of Polymer Electrolyte Fuel Cell Durability and Degradation. *Chem. Rev.* **2007**, *107*, 3904−3951.

(18) Hodnik, N.; Zorko, M.; Jozinović, B.; Bele, M.; Dražič, G.; Hočevar, S.; Gaberšček, M. Severe Accelerated Degradation of PEMFC Platinum Catalyst: A Thin Film IL-SEM Study. *Electrochem. Commun.* **2013**, *30*, 75−78.

(19) Chheda, J. N.; Huber, G. W.; Dumesic, J. A. Liquid-Phase Catalytic Processing of Biomass-Derived Oxygenated Hydrocarbons to Fuels and Chemicals. *Angew. Chem., Int. Ed.* **2007**, *46*, 7164−7183.

(20) Jin, X.; Dang, L.; Lohrman, J.; Subramaniam, B.; Ren, S.; Chaudhari, R. V. Lattice-Matched Bimetallic CuPd-Graphene Nanocatalysts for Facile Conversion of Biomass-Derived Polyols to Chemicals. *ACS Nano* **2013**, *7*, 1309−1316.

(21) Zhang, Z.; Deng, K. Recent Advances in the Catalytic Synthesis of 2, 5-Furandicarboxylic Acid and Its Derivatives. *ACS Catal.* **2015**, *5*, 6529−6544.

(22) De Jonge, N.; Ross, F. M. Electron Microscopy of Specimens in Liquid. *Nat. Nanotechnol.* **2011**, *6*, 695−704.

(23) Yuk, J. M.; Park, J.; Ercius, P.; Kim, K.; Hellebusch, D. J.; Crommie, M. F.; Lee, J. Y.; Zettl, A.; Alivisatos, A. P. High-Resolution EM of Colloidal Nanocrystal Growth Using Graphene Liquid Cells. *Science* **2012**, *336*, 61−64.

(24) Sacci, R. L.; Dudney, N. J.; More, K. L.; Parent, L. R.; Arslan, I.; Browning, N. D.; Unocic, R. R. Direct Visualization of Initial SEI Morphology and Growth Kinetics During Lithium Deposition by in Situ Electrochemical Transmission Electron Microscopy. *Chem. Commun.* **2014**, *50*, 2104−2107.

(25) Smeets, P. J. M.; Cho, K. R.; Kempen, R. G. E.; Sommerdijk, N. A. J. M.; De Yoreo, J. J. Calcium Carbonate Nucleation Driven by Ion Binding in a Biomimetic Matrix Revealed by in Situ Electron Microscopy. *Nat. Mater.* **2015**, *14*, 394−399.

(26) De Jonge, N.; Peckys, D. B.; Kremers, G. J.; Piston, D. W. Electron Microscopy of Whole Cells in Liquid with Nanometer Resolution. *Proc. Natl. Acad. Sci. U.S.A.* **2009**, *106*, 2159−2164.
(27) Zheng, H.; Smith, R. K.; Jun, Y.-w.; Kisielowski, C.; Dahmen, U.; Alivisatos, A. P. Observation of Single Colloidal Platinum Nanocrystal Growth Trajectories. *Science* **2009**, *324*, 1309−1312.
(28) Alloyeau, D.; Dachraoui, W.; Javed, Y.; Belkahla, H.; Wang, G.; Lecoq, H.; Ammar, S.; Ersen, O.; Wisnet, A.; Gazeau, F.; et al. Unravelling Kinetic and Thermodynamic Effects on the Growth of Gold Nanoplates by Liquid Transmission Electron Microscopy. *Nano Lett.* **2015**, *15*, 2574−2581.
(29) Radisic, A.; Vereecken, P. M.; Hannon, J. B.; Searson, P. C.; Ross, F. M. Quantifying Electrochemical Nucleation and Growth of Nanoscale Clusters Using Real-Time Kinetic Data. *Nano Lett.* **2006**, *6*, 238−242.
(30) Lu, Y.; Geng, J.; Wang, K.; Zhang, W.; Ding, W.; Zhang, Z.; Xie, S.; Dai, H.; Chen, F.-R.; Sui, M. Modifying Surface Chemistry of Metal Oxides for Boosting Dissolution Kinetics in Water by Liquid Cell Electron Microscopy. *ACS Nano* **2017**, *11*, 8018−8025.
(31) Meijerink, M. J.; De Jong, K. P.; Zečević, J. Assessment of Oxide Nanoparticle Stability in Liquid Phase Transmission Electron Microscopy. *Nano Res.* **2019**, *12*, 2355−2363.
(32) Zečević, J.; Hermannsdörfer, J.; Schuh, T.; De Jong, K. P.; De Jonge, N. Anisotropic Shape Changes of Silica Nanoparticles Induced in Liquid with Scanning Transmission Electron Microscopy. *Small* **2017**, *13*, No. 1602466.
(33) Meijerink, M. J.; Spiga, C.; Hansen, T. W.; Damsgaard, C. D.; De Jong, K. P.; Zečević, J. Nanoscale Imaging and Stabilization of Silica Nanospheres in Liquid Phase Transmission Electron Microscopy. *Part. Part. Syst. Charact.* **2019**, *36*, No. 1800374.
(34) Hermannsdörfer, J.; de Jonge, N.; Verch, A. Electron Beam Induced Chemistry of Gold Nanoparticles in Saline Solution. *Chem. Commun.* **2015**, *51*, 16393−16396.
(35) Woehl, T. J.; Park, C.; Evans, J. E.; Arslan, I.; Ristenpart, W. D.; Browning, N. D. Direct Observation of Aggregative Nanoparticle Growth: Kinetic Modeling of the Size Distribution and Growth Rate. *Nano Lett.* **2014**, *14*, 373−378.
(36) Ciriminna, R.; Falletta, E.; Della Pina, C.; Teles, J. H.; Pagliaro, M. Industrial Applications of Gold Catalysis. *Angew. Chem., Int. Ed.* **2016**, *55*, 14210−14217.
(37) Haruta, M. Chance and Necessity: My Encounter with Gold Catalysts. *Angew. Chem., Int. Ed.* **2014**, *53*, 52−56.
(38) Davis, S. E.; Houk, L. R.; Tamargo, E. C.; Datye, A. K.; Davis, R. J. Oxidation of 5-Hydroxymethylfurfural over Supported Pt, Pd and Au Catalysts. *Catal. Today* **2011**, *160*, 55−60.
(39) Donoeva, B.; Masoud, N.; De Jongh, P. E. Carbon Support Surface Effects in the Gold-Catalyzed Oxidation of 5-Hydroxymethylfurfural. *ACS Catal.* **2017**, *7*, 4581−4591.
(40) Villa, A.; Dimitratos, N.; Chan-Thaw, C. E.; Hammond, C.; Veith, G. M.; Wang, D.; Manzoli, M.; Prati, L.; Hutchings, G. J. Characterisation of Gold Catalysts. *Chem. Soc. Rev.* **2016**, *45*, 4953−4994.
(41) Campbell, C. T.; Parker, S. C.; Starr, D. E. The Effect of Size-Dependent Nanoparticle Energetics on Catalyst Sintering. *Science* **2002**, *298*, 811−814.
(42) Parker, S. C.; Campbell, C. T. Reactivity and Sintering Kinetics of Au/TiO_2 (110) Model Catalysts: Particle Size Effects. *Top. Catal.* **2007**, *44*, 3−13.
(43) Block, B. P.; Bailar, J. C., Jr. The Reaction of Gold (III) with Some Bidentate Coördinating Groups. *J. Am. Chem. Soc.* **1951**, *73*, 4722−4725.
(44) Zhu, H.; Ma, Z.; Clark, J. C.; Pan, Z.; Overbury, S. H.; Dai, S. Low-Temperature CO Oxidation on Au/Fumed SiO_2-Based Catalysts Prepared from $Au(en)_2Cl_3$ Precursor. *Appl. Catal., A* **2007**, *326*, 89−99.
(45) Schneider, N. M.; Norton, M. M.; Mendel, B. J.; Grogan, J. M.; Ross, F. M.; Bau, H. H. Electron−Water Interactions and Implications for Liquid Cell Electron Microscopy. *J. Phys. Chem. C* **2014**, *118*, 22373−22382.
(46) Bond, G. C.; Louis, C.; Thompson, D. T. *Catalysis by Gold*; Imperial College Press: London, 2006; Vol. *6*.
(47) Carabineiro, S. A. C.; Silva, A. M. T.; Dražić, G.; Tavares, P. B.; Figueiredo, J. L. Effect of Chloride on the Sinterization of Au/CeO_2 Catalysts. *Catal. Today* **2010**, *154*, 293−302.
(48) De Jonge, N. Theory of the Spatial Resolution of (Scanning) Transmission Electron Microscopy in Liquid Water or Ice Layers. *Ultramicroscopy* **2018**, *187*, 113−125.
(49) Wynblatt, P.; Gjostein, N. A. Supported Metal Crystallites. *Prog. Solid State Chem.* **1975**, *9*, 21−58.
(50) Haynes, W. M. *CRC Handbook of Chemistry and Physics*; CRC Press: New York, 2014; Vol. *95*.
(51) Henglein, A. Small-Particle Research: Physicochemical Properties of Extremely Small Colloidal Metal and Semiconductor Particles. *Chem. Rev.* **1989**, *89*, 1861−1873.
(52) Ivanova, O. S.; Zamborini, F. P. Electrochemical Size Discrimination of Gold Nanoparticles Attached to Glass/Indium-Tin-Oxide Electrodes by Oxidation in Bromide-Containing Electrolyte. *Anal. Chem.* **2010**, *82*, 5844−5850.
(53) Henglein, A.; Linnert, T.; Mulvaney, P. Reduction of Ag^+ in Aqueous Polyanion Solution: Some Properties and Reactions of Long-Lived Oligomeric Silver Clusters and Metallic Silver Particles. *Ber. Bunsen-Ges. Phys. Chem.* **1990**, *94*, 1449−1457.
(54) Mulvaney, P.; Linnert, T.; Henglein, A. Surface Chemistry of Colloidal Silver in Aqueous Solution: Observations on Chemisorption and Reactivity. *J. Phys. Chem. A.* **1991**, *95*, 7843−7846.
(55) Woehl, T. J.; Evans, J. E.; Arslan, I.; Ristenpart, W. D.; Browning, N. D. Direct in Situ Determination of the Mechanisms Controlling Nanoparticle Nucleation and Growth. *ACS Nano* **2012**, *6*, 8599−8610.
(56) Munnik, P.; Velthoen, M. E. Z.; De Jongh, P. E.; De Jong, K. P.; Gommes, C. J. Nanoparticle Growth in Supported Nickel Catalysts During Methanation Reaction—Larger Is Better. *Angew. Chem., Int. Ed.* **2014**, *53*, 9493−9497.
(57) Ben-Jacob, E.; Garik, P. The Formation of Patterns in Non-Equilibrium Growth. *Nature* **1990**, *343*, 523−530.
(58) Van den Berg, R.; Parmentier, T. E.; Elkjær, C. F.; Gommes, C. J.; Sehested, J.; Helveg, S.; De Jongh, P. E.; De Jong, K. P. Support Functionalization to Retard Ostwald Ripening in Copper Methanol Synthesis Catalysts. *ACS Catal.* **2015**, *5*, 4439−4448.

https://dx.doi.org/10.1021/acs.jpcc.9b10237
J. Phys. Chem. C 2020, 124, 2202−2212